DOI: 10.21062/mft.2023.109 http://www.journalmt.com

Design of a Biped Climbing Robot: Simulation, Comparison and Implementation

Tao Huang (0000-0002-9244-1203)[1,2], Rundong Cao (0009-0000-3556-8219)[3], Xinliang Wu (0009-0005-5181-3276)[4]
[1]Modern Engineering Training Center, Xiamen University of Technology. 600 Ligong Road, Xiamen City, Fujian Province. China. E-mail: tao_huang@foxmail.com
[2]Xiamen Key Laboratory of Frontier Electric Power Equipment and Intelligent Control, Xiamen City, Fujian Province. China.
[3]Ruijie Networks Co., Ltd. Building 19, Juyuanzhou Industrial Park, No. 618 Jinshan Avenue, Cangshan District, Fuzhou City, Fujian Province. China. E-mail: rundong_cao@163.com
[4]Modern Engineering Training Center, Xiamen University of Technology. 600 Ligong Road, Xiamen City, Fujian Province. China. E-mail: E-mail: xlwu@xmut.edu.cn

In this paper, the design of a robot is proposed to replace manual labor in completing tasks on vertical planes. The aim is to enhance automation in the workplace and eliminate direct human involvement to ensure personal safety. Firstly, the robot's structure is designed as a five-joint biped with vacuum adsorption capabilities. The forward and inverse kinematics of the robot are analyzed. Secondly, using simulation by ADAMS, five key performance metrics are quantitatively analyzed for both this robot and a Hexapod robot. These metrics include adsorption reliability, external load-bearing capacity, friction coefficient adaptability, obstacle-crossing capacity, and joint torque. Thirdly, the main control chip used for this robot is STM32F407. The circuit system design and physical implementation of the robot are based on this chip. Finally, experiments are conducted to study the actual performance of the robot in vertical cleaning tasks.

Keywords: Wall-climbing robot, biped robot, vertical cleaning

1 Introduction

With the rapid development of society and the continuous improvement of land utilization rates, both residential and commercial buildings have witnessed significant increases in height and density, leading to increasingly complex building structures. Consequently, there is a growing demand for efficient cleaning of vertical surfaces such as high-rise glass and indoor walls, accompanied by increased associated risks. Human labor alone cannot meet these social needs. Hence, this paper aims to design a climbing robot that can replace manual methods of vertical surface cleaning promoting personal safety and enhancing work efficiency. The development of such a climbing robot necessitates establishing stable adsorption performance and the subsequent development of the cleaning system. Scholars in the field have extensively investigated two critical functions of the climbing robot: adsorption and movement. According to the adsorption mode, it can be classified into various types: permanent magnetic adsorption, electromagnetic adsorption, inter-molecular force, negative pressure, vacuum adsorption, and composite. Based on the movement mode, it can be categorized as wheel type, foot type, crawler type, rope type, and compound type. From a bionics perspective, Shiyuan Bian et al. [1] developed a quadruped crawling robot inspired by geckos' bristle climbing mechanism. However, this robot has limited load capacity and is equipped with a limited number of execution devices; therefore, it is suitable for reconnaissance and survey purposes. In the field of ferromagnetic wall defect detection, the most commonly used structure is the permanent magnet adsorption wheel: Qiu et al. [2] conducted simulation analysis and experimental demonstration to study the running state of a magnetic robot near dangerous points; Li et al. [3] analyzed the adsorption stability of an ultrasonic wall climbing robot under various working conditions through simulation and verified the results through experiments; References [4,5] improved the robot's adsorption capacity by optimizing its structure and enhancing magnetic energy efficiency; References [6,7] proposed solutions for tracking problems and 2D direction angle detection encountered by climbing robots during movement while optimizing path planning in their climbing process. In the presence of a ferromagnetic surface, foot structures exhibit a superior ability to navigate facade obstacles compared to wheel structures. Lv et al. [8] conducted a comprehensive analysis of the stability and dynamics of foot structures

on magnetic surfaces, laying a solid theoretical foundation for practical applications. Conversely, when the facade upon which the robot operates is non-ferromagnetic, the robot cannot leverage magnetic attraction to counteract gravity. Studies [9-13] have introduced climbing robots tailored for specific environments, including bridges, hulls, ceiling plates, and poles. Sungkeun Yoo et al. [14,15] presented a wall-climbing platform powered by ropes and propellers. This platform boasts a robust load capacity and the ability to traverse large gaps. However, its size restricts its efficacy in certain scenarios, such as cleaning wall corners. The crawler structure, introduced by Hu et al. [16] and Guo et al. [17], represents a notable advancement in climbing robot design. It can be viewed as an enhancement of the wheel structure, with improved capabilities in spanning vertical planes. Robots with vacuum adsorption foot structures typically have a moderate size, allowing for intricate gaits and multi-directional movement. They are particularly apt for cleaning high-rise exteriors with non-ferromagnetic structures. Zhang et al. [18] conducted experiments demonstrating the viability of vacuum adsorption bipedal robots. While references [19,20] delved into the optimal design of climbing gaits for these robots, there remains a gap in comparative simulations and experimental validations concerning the influence of robot structure on performance. In this paper, we accomplished several objectives:

- A vacuum adsorption biped robot with five joints tailored for vertical plane cleaning applications is designed. The forward and inverse kinematics of this robot were thoroughly analyzed.
- Using ADAMS simulation, we quantitatively assessed key parameters of both the vacuum adsorption hexapod and bipedal structures. These parameters include adsorption reliability, external load-bearing capacity, adaptability to varying friction coefficients, obstacle traversal capability, and joint torque.
- We developed a circuit system for the biped climbing robot, employing the STM32F407 as the primary control chip.
- Experimental evaluations were conducted to validate the performance of the bipedal vacuum adsorption climbing robot in vertical surface cleaning tasks. These evaluations focused on adsorption stability, adaptability to vertical surfaces, and the ability to overcome obstacles on vertical planes.

The findings presented in this paper lay a solid foundation for devising more effective implementation strategies for climbing robots.

2 Materials and Methods

2.1 Design of System Structure

The climbing robot is designed not only to traverse smoothly across flat facades with varying friction coefficients but also to bear a specific external load. In environments such as window sills and wall corners, where the robot is expected to navigate obstacles or transition between walls, enhanced mobility is essential. When considering control mechanisms, a bipedal climbing robot offers a more straightforward gait and more intuitive control logic compared to its multi-legged counterparts. Kinematically speaking, the bipedal design provides greater flexibility and superior climbing capabilities, aligning well with the requirements of wall cleaning, as cited in references [19,21]. Consequently, this section introduces the design of a vacuum-adhesion bipedal climbing robot. This robot, reminiscent of a creeping reptile, features five joints. Fig. 1 illustrates its mechanical motion diagram. By manipulating the translation and rotation of the D-H coordinate system for each joint, one can derive the matrix representing the end-effector's coordinate system relative to the base, which is crucial for the physical system's design. [24-26]

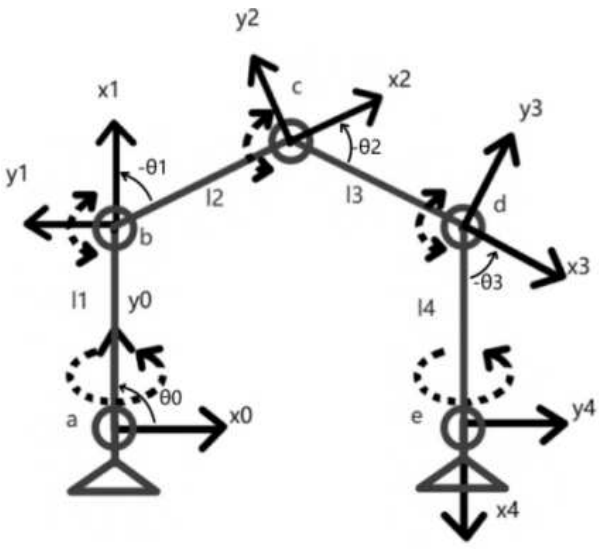

Fig. 1 *Joints' Diagram and Coordinates of Biped Robot*

As shown in Fig. 1, red circles labeled from 'a' to 'e' represent the column hinge joints. The black dotted lines signify the rotation direction of these column hinges. Specifically, the rotation axis for hinge 'a' is y_0, while hinges 'b' to 'd' have rotation axes corresponding to z_1 through z_3. The rotation axis for hinge 'e' is x_4. It's worth noting that the z-axis, which constitutes the third coordinate axis in the three-dimensional rotating system, is absent from the figure. The lengths of the

connecting rods are denoted by 'l1' through 'l4'. The red triangle symbolizes the executive end, encompassing both the adsorption and cleaning devices. The angle θ_n is defined as the angle between the coordinate axis x_n and l_{n+1}, where 'n' is an integer ranging from 0 to 4, representing joints 0 through 4. The origin of the coordinate system {0} and the connecting coordinate systems {1}-{4} are anchored at the connection points of each joint and rod. The coordinate systems depicted in Fig. 1 adhere to the specifications of $\vec{x}_n \times \vec{y}_n = \vec{z}_n$.

Note the rotation angle of column hinge 'a' or 'e' in the direction of the black dotted line, as shown in Fig. 1, denoted as θ_a and θ_e respectively. These angles represent the included angle between z_1 and z_0, and the included angle between z_4 and z_3. The homogeneous transformation matrix of the end coordinate system {4} with respect to the origin coordinate system {0} can be obtained through forward kinematics when the parameters of each connecting rod and column hinge are known. The D-H parameters for the biped robot designed in this paper are presented in Tab. 1.

Tab. 1 *D-H Parameters of Designed Biped Robot*

L	**Length(mm)**	θ_z	θ_x	θ_n (°)
1	0	θ_a	0	90
2	131.7	0	0	θ_1
3	131.7	0	0	θ_2
4	0	θ_e	0	θ_3

In Tab. 1, '*L*' refers to the number of connecting rods; 'Length' represents the distance between adjacent z axes, which corresponds to the length of a connecting rod; θ_z denotes the torsion angle between adjacent z axes. It is important to note that H_n^{n-1} represents the homogeneous transformation matrix of coordinate system {n} relative to {n-1}. Moreover, the homogeneous transformation matrix of the end coordinate system {4} with respect to the origin coordinate system {0} satisfies Equation (1).

$$H_4^0 = H_1^0 \bullet H_2^1 \bullet H_3^2 \bullet H_4^3 \tag{1}$$

The translation transformation, expressing P_n^{n-1}, represents the position of coordinate system {n} relative to {n-1}, while R_n^{n-1} denotes the rotation transformation indicating its attitude. The relationship between the homogeneous transformation matrix and position and attitude is governed by Equation (2).

$$H_4^0 = \begin{bmatrix} R_4^0 & P_4^0 \\ 0 & 1 \end{bmatrix} = \prod_{n=1}^{n=4} \begin{bmatrix} R_n^{n-1} & P_n^{n-1} \\ 0 & 1 \end{bmatrix} \tag{2}$$

The rotation transformation is denoted as 'Rot', and the translation transformation is denoted as 'Trans'. The position and attitude of each transformation coordinate system {n} relative to {n-1} satisfy Equations (3) and (4).

$$R_n^{n-1} = \mathrm{Rot}_{z,\theta_z} \mathrm{Rot}_{y,\theta_y} \mathrm{Rot}_{x,\theta_x} = \begin{bmatrix} x_n \bullet x_{n-1} & x_n \bullet y_{n-1} & x_n \bullet z_{n-1} \\ y_n \bullet x_{n-1} & y_n \bullet y_{n-1} & y_n \bullet z_{n-1} \\ z_n \bullet x_{n-1} & z_n \bullet y_{n-1} & z_n \bullet z_{n-1} \end{bmatrix} \tag{3}$$

$$P_n^{n-1} = \mathrm{Trans}_z \bullet \mathrm{Trans}_x \bullet \mathrm{Trans}_y = \begin{bmatrix} \mathrm{d}x \\ \mathrm{d}y \\ \mathrm{d}z \end{bmatrix} \tag{4}$$

For convenience, $\sin\theta$ is abbreviated as $s\theta$, and $\cos\theta$ is abbreviated as $c\theta$. By using MATLAB to substitute the parameters in Tab. 1 into Equations (2), (3), and (4), Equation (5) can be obtained.

$$H_4^0 = \begin{bmatrix} \begin{bmatrix} 0 & -1 & 0 \\ 1 & 0 & 0 \\ 0 & 0 & 1 \end{bmatrix} \begin{bmatrix} 1 & 0 & 0 \\ 0 & c\theta_a & -s\theta_a \\ 0 & s\theta_a & c\theta_a \end{bmatrix} \begin{bmatrix} 0 \\ 0 \\ 0 \end{bmatrix} \\ 0 \quad 0 \quad 0 \quad 1 \end{bmatrix} \bullet$$
$$\begin{bmatrix} \begin{bmatrix} c\theta_1 & -s\theta_1 & 0 \\ s\theta_1 & c\theta_1 & 0 \\ 0 & 0 & 1 \end{bmatrix} \begin{bmatrix} 131.7c\theta_1 \\ 131.7s\theta_1 \\ 0 \end{bmatrix} \\ 0 \quad 0 \quad 0 \quad 1 \end{bmatrix} \begin{bmatrix} \begin{bmatrix} c\theta_2 & -s\theta_2 & 0 \\ s\theta_2 & c\theta_2 & 0 \\ 0 & 0 & 1 \end{bmatrix} \begin{bmatrix} 131.7c\theta_2 \\ 131.7s\theta_2 \\ 0 \end{bmatrix} \\ 0 \quad 0 \quad 0 \quad 1 \end{bmatrix} \bullet \begin{bmatrix} \begin{bmatrix} c\theta_3 & -s\theta_3 & 0 \\ s\theta_3 & c\theta_3 & 0 \\ 0 & 0 & 1 \end{bmatrix} \begin{bmatrix} 1 & 0 & 0 \\ 0 & -c\theta_e & s\theta_e \\ 0 & -s\theta_e & c\theta_e \end{bmatrix} \begin{bmatrix} 0 \\ 0 \\ 0 \end{bmatrix} \\ 0 \quad 0 \quad 0 \quad 1 \end{bmatrix} \tag{5}$$

The inverse kinematics problem is solved based on the analytical foundation of forward kinematics. It is known that the homogeneous transformation matrix of the biped climbing robot's end effector {4} relative to {0} is expressed as equation (6).

Each parameter in Equation (6) is calculated using Equation (5), and the calculation result is shown in Equation (7).

$$H_4^0 = \begin{bmatrix} n_x & s_x & a_x & d_x \\ n_y & s_y & a_y & d_y \\ n_z & s_z & a_z & d_z \\ 0 & 0 & 0 & 1 \end{bmatrix} \tag{6}$$

$$\begin{cases} n_x = c\theta_3*(c\theta_a*c\theta_1*s\theta_2 + c\theta_a*c\theta_2*s\theta_1) - s\theta_3*(c\theta_a*c\theta_1*c\theta_2 - c\theta_a*s\theta_1*s\theta_2) \\ n_y = c\theta_3*(c\theta_1*c\theta_2 - s\theta_1*s\theta_2) - s\theta_3*(c\theta_1*s\theta_2 + c\theta_2*s\theta_1) \\ n_z = c\theta_3*(s\theta_a*c\theta_1*s\theta_2 + s\theta_a*c\theta_2*s\theta_1) - s\theta_3*(s\theta_a*s\theta_1*s\theta_2 - s\theta_a*c\theta_1*c\theta_2) \\ s_x = c\theta_e*c\theta_3*(c\theta_a*c\theta_1*c\theta_2 - c\theta_a*s\theta_1*s\theta_2) - s\theta_a*s\theta_e - c\theta_e*s\theta_3*(c\theta_a*c\theta_1*s\theta_2 + c\theta_a*c\theta_2*s\theta_1) \\ s_y = c\theta_e*c\theta_3*(c\theta_1*s\theta_2 + c\theta_2*s\theta_1) + c\theta_e*s\theta_3*(c\theta_1*c\theta_2 - s\theta_1*s\theta_2) \\ s_z = c\theta_e*c\theta_3*(s\theta_a*s\theta_1*s\theta_2 - s\theta_a*c\theta_1*c\theta_2) - c\theta_a*s\theta_e + c\theta_e*s\theta_3*(s\theta_a*c\theta_1*s\theta_2 + s\theta_a*c\theta_2*s\theta_1) \\ a_x = c\theta_e*s\theta_a - s\theta_e*c\theta_3*(c\theta_a*c\theta_1*c\theta_2 - c\theta_a*s\theta_1*s\theta_2) + s\theta_e*s\theta_3*(c\theta_a*c\theta_1*s\theta_2 + c\theta_a*c\theta_2*s\theta_1) \\ a_y = -s\theta_e*c\theta_3*(c\theta_1*s\theta_2 + c\theta_2*s\theta_1) - s\theta_e*s\theta_3*(c\theta_1*c\theta_2 - s\theta_1*s\theta_2) \\ a_z = c\theta_a*c\theta_e - s\theta_e*c\theta_3*(s\theta_a*s\theta_1*s\theta_2 - s\theta_a*c\theta_1*c\theta_2) - s\theta_e*s\theta_3*(s\theta_a*c\theta_1*s\theta_2 + s\theta_a*c\theta_2*s\theta_1) \\ d_x = -131.7*c\theta_a*s\theta_1 - 131.7*c\theta_a*c\theta_1*s\theta_2 - 131.7*c\theta_a*c\theta_2*s\theta_1 \\ d_y = 131.7*c\theta_1 + 131.7*c\theta_1*c\theta_2 - 131.7*s\theta_1*s\theta_2 \\ d_z = 131.7*s\theta_a*s\theta_1 + 131.7*s\theta_a*c\theta_1*s\theta_2 + 131.7*s\theta_a*c\theta_2*s\theta_1 \end{cases} \tag{7}$$

In the robot design, based on the aforementioned kinematics analysis results, the spatial position of the joint link's end relative to the base coordinate system {0} can be established by substituting the rotation angle of each revolute joint into equation (7).

3 Discussion of results

3.1 Dynamics Simulation

3.1.1 Establishment of Simulation Model

According to research referenced in [9], multi-legged robots exhibit similar functions with six-legged robots being more flexible and stable compared to four-legged ones. In this section, taking the hexapod robot as a reference object, a quantitative analysis is performed through simulation to evaluate the advantages and disadvantages of the bipedal robot in vertical movement. SolidWorks software is utilized for modeling both robots. The volume size of each robot does not exceed 110*300*250 (mm). Additionally, each suction cup has a radius of 30 mm. Fig. 2 illustrates that each foot of the Hexapod structure consists of three rotating pairs, three connecting rods, a vacuum sucker connected at the end of connecting rod *n*-(1), and a body connected at the end of connecting rod *n*-(3). The vacuum pump is placed within the body (not shown in the figure). Fig. 3 depicts that the bipedal structure comprises five rotating pairs, two connecting rods, and two sets of vacuum pumps and vacuum suckers at the end of each rotating pair.

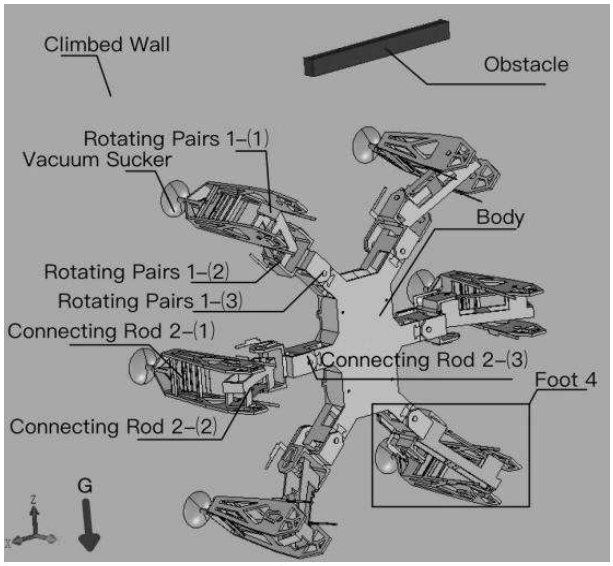

Fig. 2 *Structure diagram of Hexapod Robot*

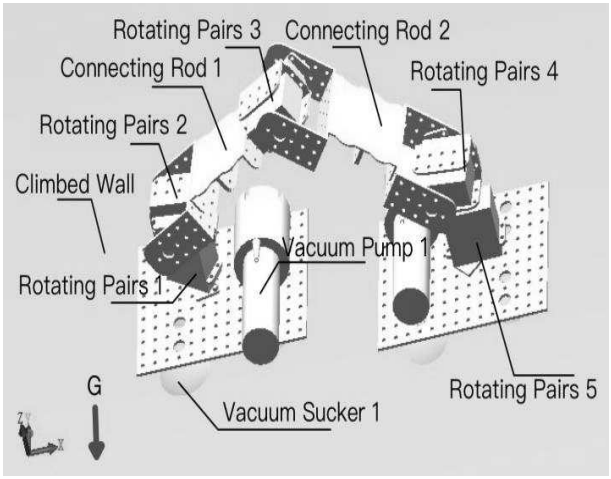

Fig. 3 *Structure Diagram of Biped Robot*

The topological structures of the two robot models are similar, consisting of a vacuum pump, vacuum suckers, rotating pairs (steering engines), connecting rods, and body. However, there is a difference in their structures: the Hexapod structure is hybrid while the biped structure is series. The structural materials used for the robot bodies designed in ADAMS are aluminum alloys with a material density of approximately 2.8 g/cm^3. The weights assigned to different parts of the robot are as follows: robot control circuit (700g), task-performing devices such as cleaning mechanisms (200g), a single steering engine (230g), and a single vacuum pump (300g). The vacuum degree is set at -70Kpa. Furthermore, Tab. 2 presents the contact parameters between the sucker surface and climbed wall.

Tab. 2 *The Contact Parameters Between Sucker Surface and Climbed Wall*

Rigidity	Force index	Damping unit: N/(m/s)	Penetration Depth unit: mm	Adsorption Force (Contact) unit: N	Static Friction Coefficient	Dynamic Friction Coefficient	Static Translation Velocity unit: mm/s	Friction Translation Speed unit: mm/s	Adsorption Force (Non-conta-ct) unit: N
1000	2.2	100	0.1	198.5	0.5	0.4	100	1000	0

3.1.2 Dynamic simulation

Dynamic simulation is conducted for both robots, considering the reduction of irrelevant variables during gait design. Additionally, each robot has three working suckers in contact with the wall. Therefore, the simulation hexapod robot adopts a waveform gait with a stable stride (triangular gait) based on reference [21], which provides specific kinematics analysis and displays key-frames in Fig. 4.

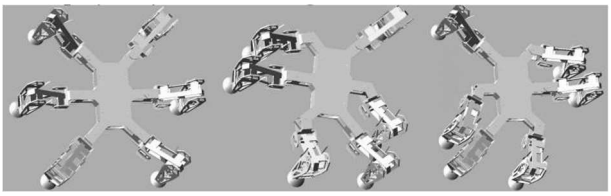

Fig. 4 *Gait Keyframes of Hexapod Robot*

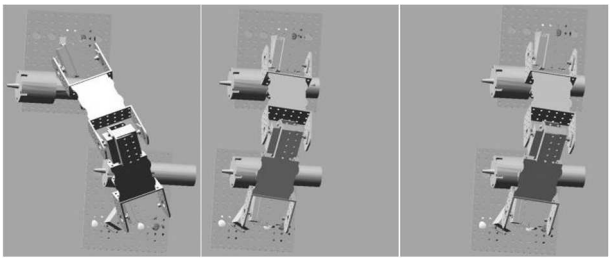

Fig. 5 *Gait Keyframes of Biped Robot*

Research on biped robot gaits is relatively limited, mostly focusing on anthropomorphic walking [22,23], wheel leg [18], or peristaltic gaits [19,27]. Considering previous research and work requirements, the biped robot is designed with a walking peristaltic hybrid gait. The key-frame for this gait is shown in Fig. 5.

3.1.3 Experiment 1

- Premise: Constant adsorption force;
- Purpose: Investigate how changes in friction coefficient or external load affect the motion of the robot; specifically studying time-varying loads when operating on different material surfaces.

Experimental conditions:

- (1) Under reference conditions described in section 3.1.
- (2) With an additional 2kg load.
- (3) When the static friction coefficient drops to 0.4.
- (4) When the friction coefficient is reduced to 0.3.

Output: Displacement of the robot body in the direction of positive work due to gravity.

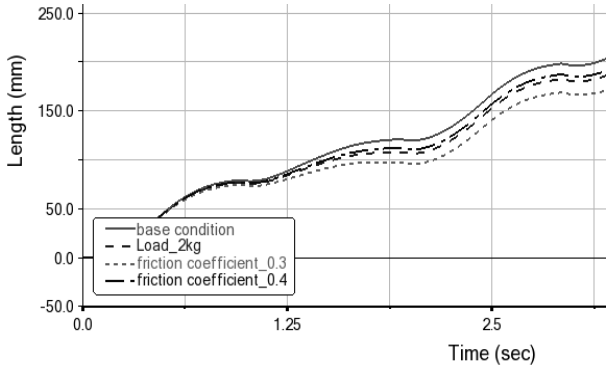

Fig. 6 *Displacement Waveform of Hexapod Robot*

Fig. 6 illustrates the displacement waveform of the hexapod robot in the simulation experiment. The red solid line, blue dotted line, black dotted line, and pink imaginary points in Fig. 6 and 7 correspond to experimental conditions (1), (2), (3), and (4) respectively. It can be observed from Fig. 6 that the initial and final displacement of the hexapod robot in the direction of positive work by gravity is positive, indicating that the hexapod robot can successfully perform wall climbing under these four conditions. However, under the influence of gravity, the robot experiences varying degrees of slipping under each condition, with slip accumulation over time. At 2s, the robot completes a set of gait cycle actions as depicted in Fig. 7. The amount of slip compared to the reference condition (1) is measured for different conditions:

- Condition (2) exhibits a slip of 13.3mm;
- Condition (3) shows a slip of 7.9mm;
- Condition (4) demonstrates a slip of 24mm.

Similarly, data regarding slip within 0.1s for different conditions are recorded for the hexapod robot:

- Condition (1) exhibits a slip of 1.1mm;
- Condition (2) shows a slip of 1.7mm;
- Condition (3) demonstrates a slip of 1.1mm;
- Condition (4) displays a slip of 1.8mm.

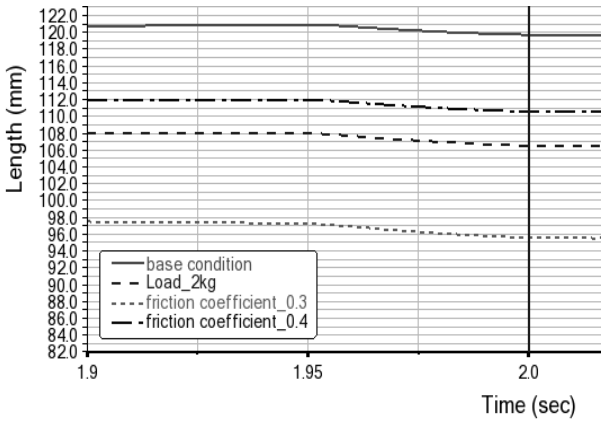

Fig. 7 *Displacement Difference of Hexapod Robot Under Four Experimental Conditions*

The measured data for the biped robot are presented in Fig. 8 and 9. It can be observed that the displacement characteristics in the direction of positive work by gravity for the biped robot are similar to those exhibited by the hexapod structure. The amount of slip compared to reference condition (1) when completing a set of gait cycle actions at time t=3s is measured:

- Condition (2) exhibits a slip of 13.4mm;
- Condition (3) shows a slip of 4.7mm;
- Condition (4) demonstrates a slip of 12mm.

Similarly, data regarding self-slip within 0.1s for different conditions are recorded for the biped robot:

- Condition (1) exhibits a sliding distance of 0.1mm;
- Condition (2) shows a slip of 0.7mm;
- Condition (3) demonstrates a slip of 0.6mm;
- Condition (4) displays a slip of 0.6mm.

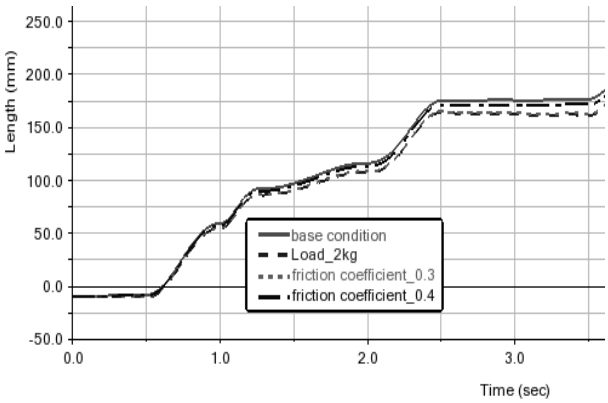

Fig. 8 *Displacement Waveform of Biped Robot*

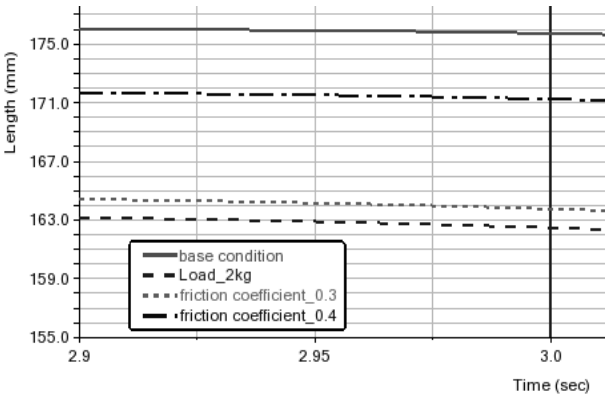

Fig. 9 *Displacement Difference of Biped Robot Under Four Experimental Conditions*

3.1.4 Experiment 2

- Purpose: Investigate the influence of obstacles on robot movement during limit crossing gait, specifically studying the robot's working ability under window sill and other conditions.
- Experimental obstacle size: 20*40*1000mm.
- Constraint condition: Ensure strict parallelism between the robot suckers and the climbed wall to ensure stable adhesion of the robot to the wall.
- Comparison: The number of collisions when the robot crosses an obstacle

ISSN 1213–2489
e-ISSN 2787–9402

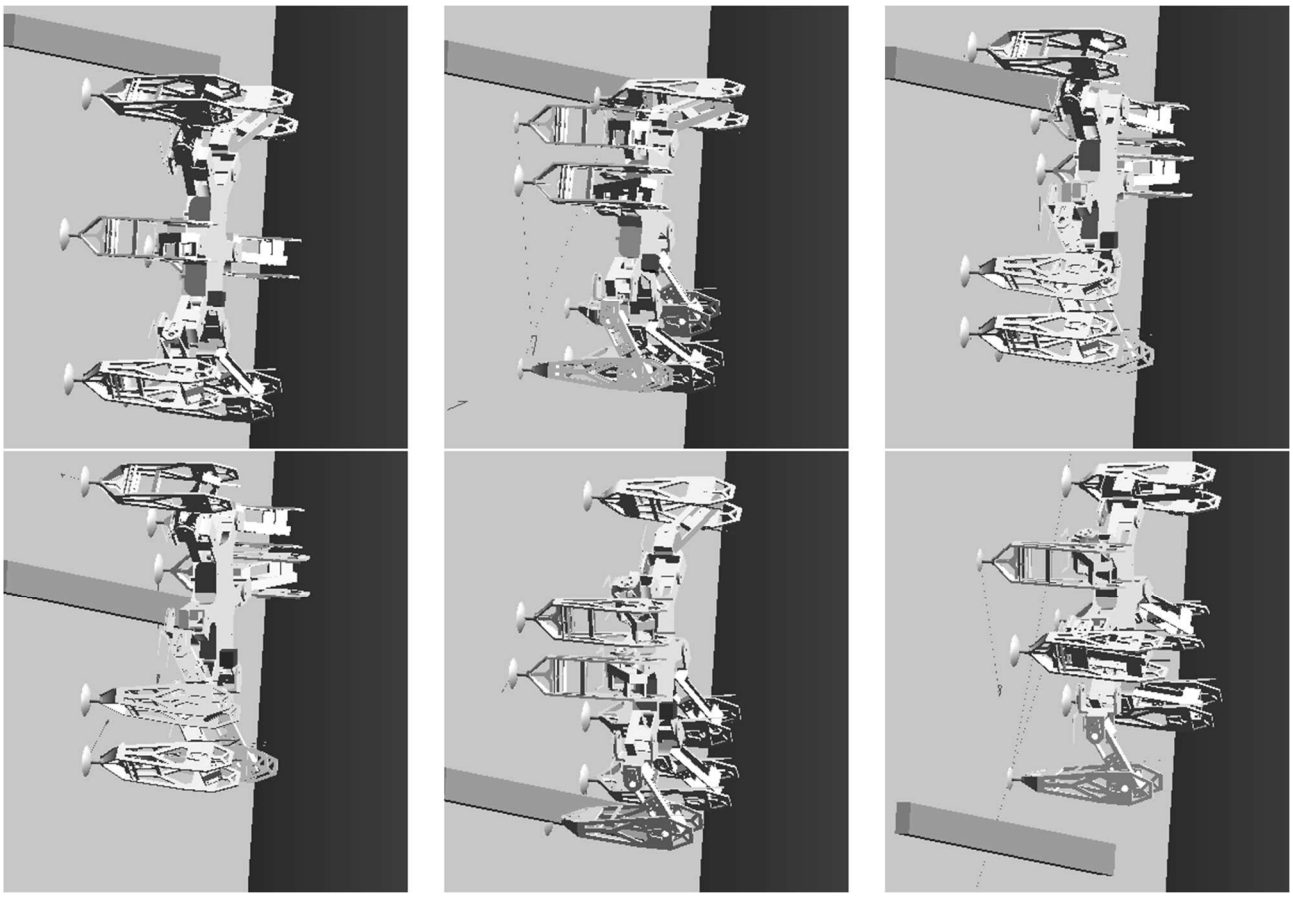

Fig. 10 *Obstacle crossing of Hexapod Robot*

After conducting numerous tests, keyframes from the hexapod robot's crossing experiment are captured and presented in Fig. 10, while key frames from the biped robot's crossing experiment are depicted in Fig. 11. The hexapod robot requires at least three gait cycles to complete a full climb and may encounter three to five collisions with obstacles during this process. On the other hand, the biped robot only needs one gait cycle to complete a full climb and may experience zero to two collisions.

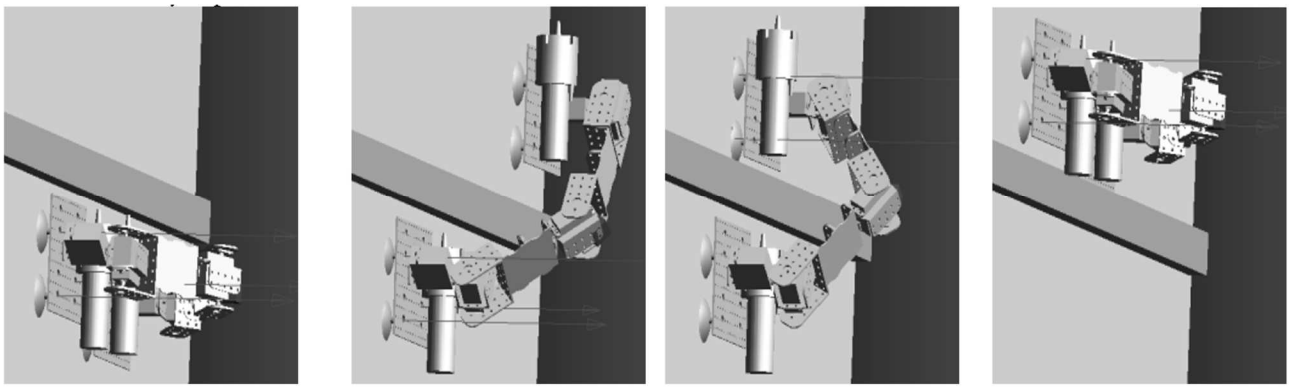

Fig. 11 *Obstacle crossing of Biped Robot*

The torque waveforms of each joint of foot 1 and foot 2, front foot and middle foot on the same side, of the hexapod robot are measured as shown in Fig. 12. The output torques of different joints of the hexapod robot are as follows:

- Instantaneous maximum output torque of Joint 2-(3): 7.7*10^4 N·mm;
- Effective value of output torque of Joint 1-(3): 5*10^4 N·mm;
- Effective value of output torque for other joints of the hexapod robot is less than 2.5*10^4 N·mm.

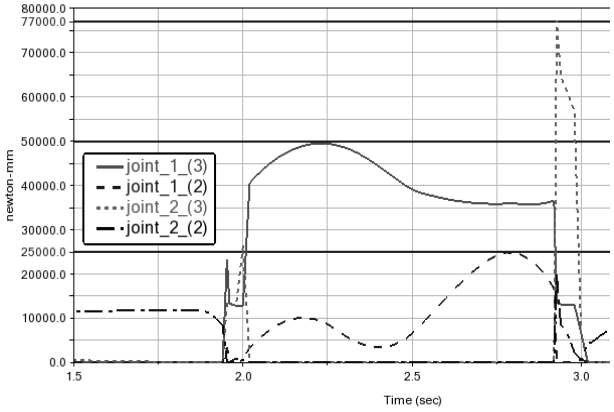

Fig. 12 *Joint Torque Waveform of Hexapod Robot*

The torque waveforms of each joint of the biped robot are measured as shown in Fig. 13. It can be observed that joint_d requires a torque of 1.25*10^5 N·mm, joint_c requires a torque of 7.5*10^4 N·mm, and the other joints need to meet a torque requirement of 2*10^4 N·mm.

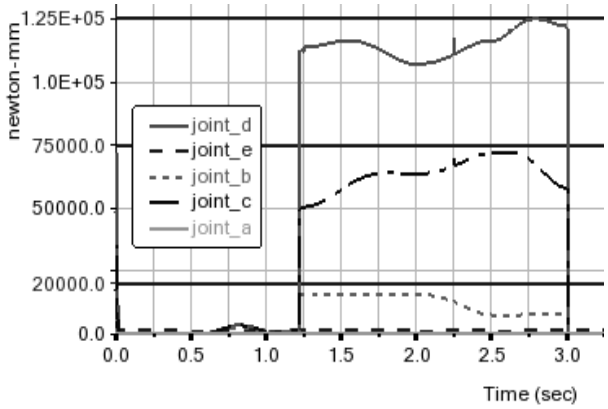

Fig. 13 *Joint Torque Waveform of Biped Robot*

When considering materials with the same density, size, and unit weight for electrical apparatus:

- With the same friction coefficient, the influence of an external load weight of 2kg on the biped structure is approximately 41% compared to that on the hexapod structure.
- With the same external load, the influence of changes in friction coefficient with medium amplitude on the biped structure is about 33.3%-54.4% compared to that on the hexapod structure.
- With both the same friction coefficient and external load, the gait performance over obstacles is much simpler for bipedal structures compared to hexapod structures, while their climbing ability is significantly higher.
- The torque amplitude for a single joint in a hexapod structure is approximately 56% compared to that in a biped structure.

3.1.5 Circuit System Design of Biped Climbing Robot

Based on the design analysis mentioned above, a biped robot with air quality detection, video monitoring, wireless communication, and vertical surface cleaning capabilities has been realized. The circuit hardware system includes the following components:

- Main control chip,
- Power circuit,
- Vacuum pump driving circuit,
- Steering engine and its control circuit.

The sensors mainly consist of an attitude sensor, an intelligent camera, an air monitoring sensor, and a wireless communication sensor. Fig. 14 illustrates the hardware structure framework of the robot. The main circuit modules include:

- Supply unit: 5V power supply and 12V power supply
- Sensor unit: (1) attitude sensor, (2) camera, (3) air monitoring, (4) ESP8266
- Main control: STM32F407ZGT6
- Operation Unit: (1) steering engine, (2) vacuum pump, (3) 2Z relay.

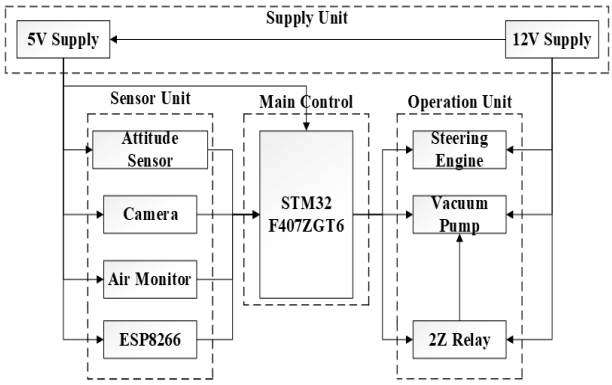

Fig. 14 *Robot Hardware Framework*

The 12V power supply is used for the operation unit, while the 5V power supply is obtained through DC-DC step-down to power the sensor unit and main control. The output of operation unit-(3) is controlled by the main control chip, and the power gain and loss of operation unit-(2) are controlled by operation unit-(3). The sensor units (1)(2)(3)(4) respectively send back signals to the main control chip including joint attitude change angle, real-time monitoring video stream, formaldehyde concentration, temperature and humidity, other air indicators, and wireless

communication data. The main control module analyzes these returned data from the sensor units and adjusts the output signal flow to control the operation unit.

The main control chip utilizes an STM32F407 single-chip microcomputer powered by a 5V power supply. The internal resource usage of this microcomputer includes: (1) using two timers to output five PWM waves for controlling steering engine actions; (2) employing two USART channels for communication with both the camera module and ESP8266 module; (3) utilizing seven IIC channels for communication with the attitude sensor module and the air detection module; (4) incorporating two push-pull output IOs to control relays and vacuum pump actions.

The attitude sensor module employs a commonly used three-axis electronic gyroscope MUP6050 to detect the real-time attitude angles of each joint on the robot. The angle data is processed by the single-chip microcomputer through the IIC bus to control the rotation of steering engines. Relays are powered by a 12V supply with optocoupler isolation, supporting high-level and low-level triggering to switch vacuum pump adsorption and release. ESP8266 is selected as the wireless communication module, enabling the connection between the STM32F4 chip and the user's wireless network signal from a mobile phone. Data packets can be sent to the Network server ONENET for wireless data monitoring. The schematic diagram of the attitude sensor, relay, and ESP8266 is shown in Fig. 15.

The schematic diagram of the steering engine is depicted in Fig. 16, with an input voltage range of 12V to 24V.

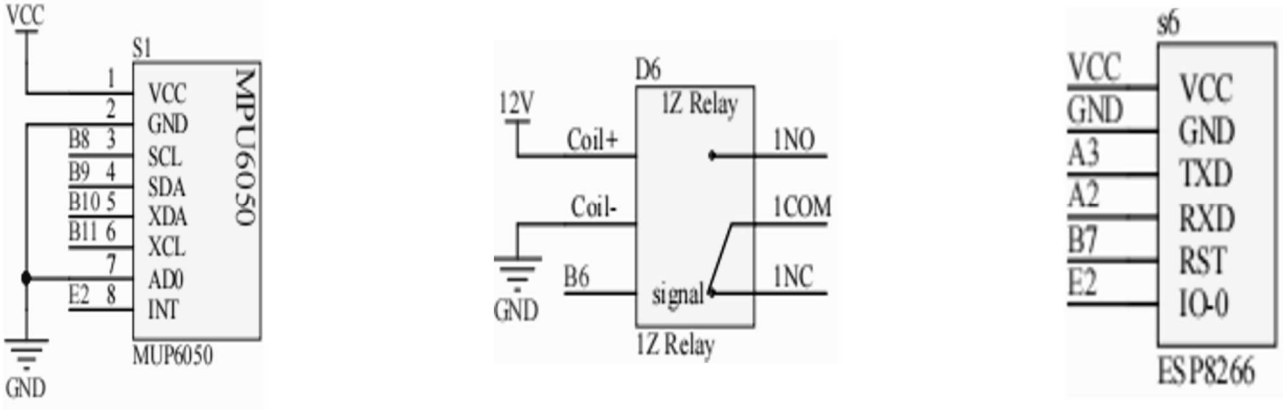

Fig. 15 *Schematic Diagram of Some Important Components*

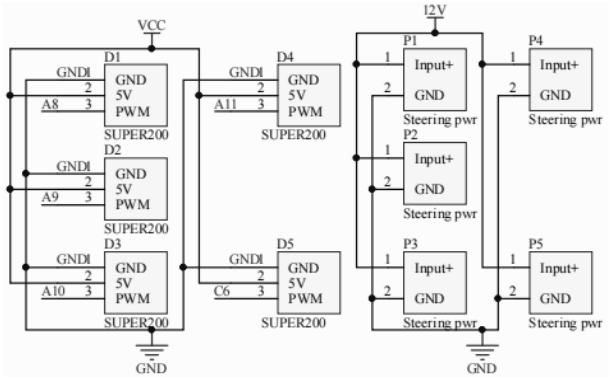

Fig. 16 *Schematic Diagram of Steering Engine*

Based on the functional requirements, the execution flow chart of the biped robot is designed as illustrated in Fig. 17. The control signal input to each steering engine by the single-chip microcomputer is a square wave signal with a constant cycle of 20ms and a duty ratio ranging from 5% to 10%. Assuming the current angle of each link is β1 and the target angle is β2, the control law is realized through incremental PID.

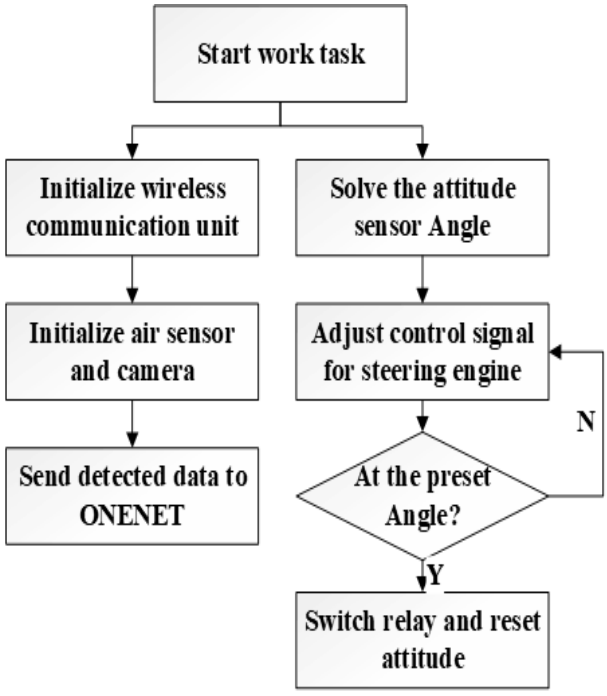

Fig. 17 *System Execution Flow Chart*

3.2 Implementation and Experiment

With reference to the above simulation results and circuit design, a biped cleaning robot with climbing function has been successfully developed. The main frame of this robot is constructed using aluminum alloy, weighing a total of 2894g and measuring at dimensions of 216*108*296mm. A physical representation of this biped climbing robot can be observed in Fig. 18.

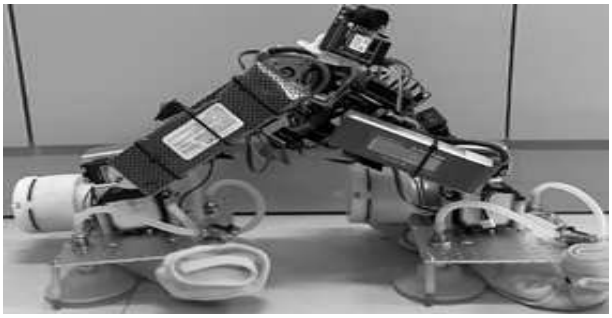

Fig. 18 *Biped Climbing Robot*

3.2.1 Experiment of Adsorption Stability and Vertical Plane Adaptability

The adsorption stability experiments were conducted under various working conditions, including the surfaces of photovoltaic panels, painted walls, wardrobe cabinets, and window glass. As depicted in Fig. 19, the climbing robot demonstrated stable adsorption without sliding in all four working conditions.

3.2.2 Experiments of Obstacle Crossing in Vertical Plane

Fig. 20 presents the experimental results of the climbing robot's ability to overcome obstacles in a vertical plane. The results indicate that the climbing robot successfully surmounted window sill obstacles with a width of 45mm and a height of 38mm. It took t=5.47s for the robot to complete one step, which corresponds to half a gait cycle. Each step covered a distance of 9.8cm, resulting in a travel speed of 1.79cm/s.

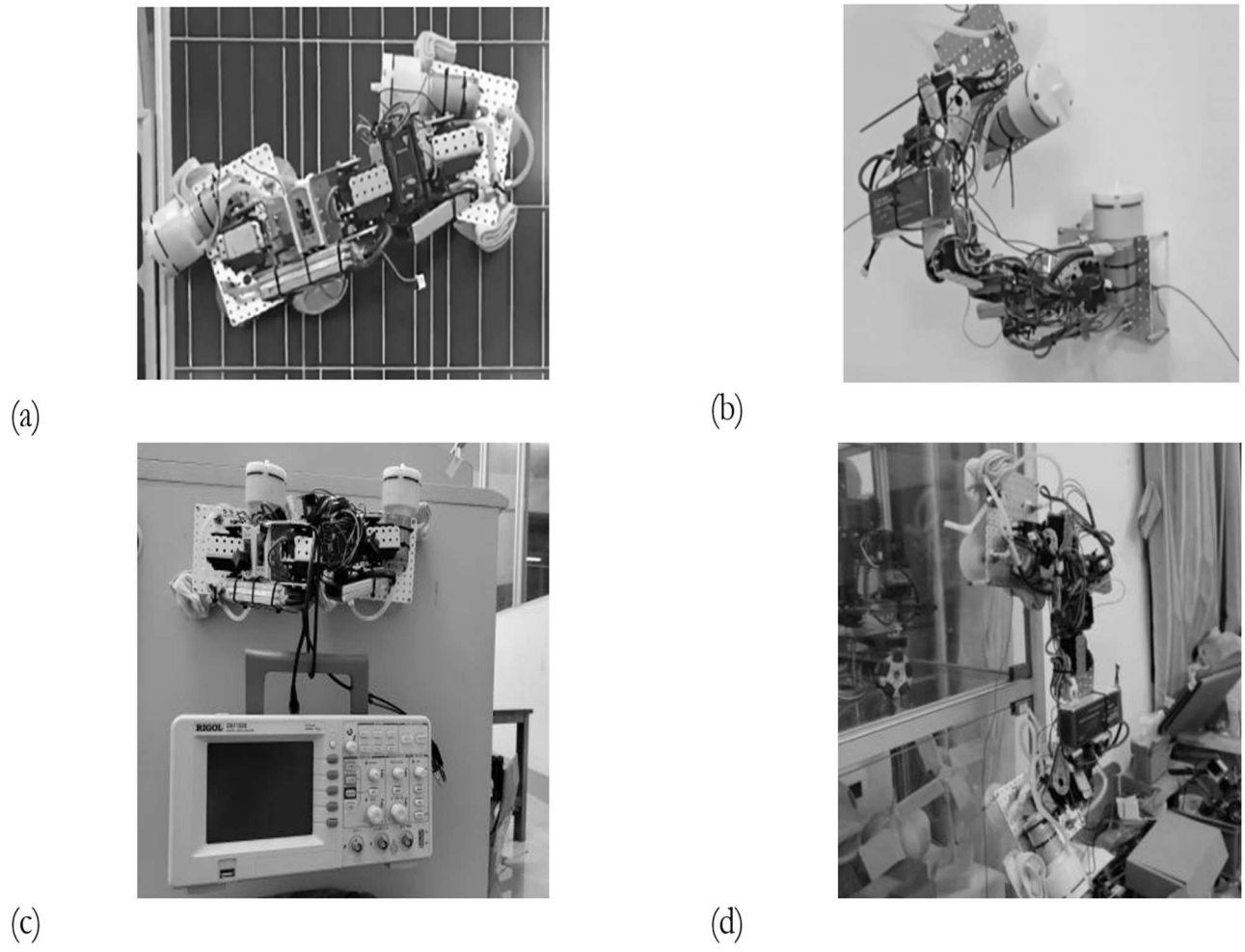

Fig. 19 *Adaptability experiments of different vertical planes: (a) Adsorption experiment of photovoltaic panel surface; (b) Adsorption experiment of a common plastered wall; (c) Load experiment of cabinet surface; (d) Experiment of single foot adsorption glass surface*

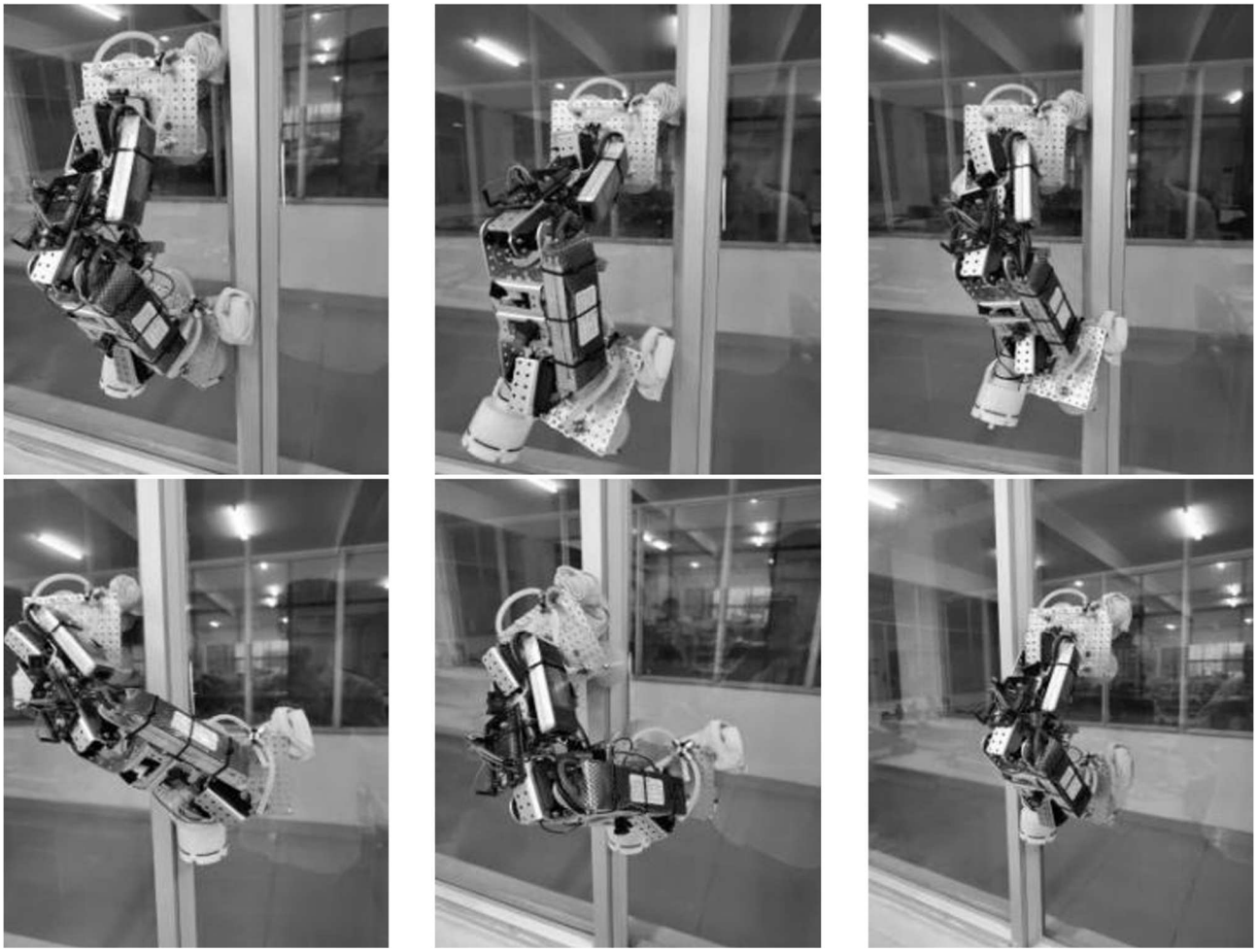

Fig. 20 *Actions of Robot Over Window Sill*

4 Conclusions

The biped climbing robot possesses several advantages over its Hexapod counterpart, such as fewer actuators and a simpler structure. Modeling and simulation using ADAMS revealed that the biped climbing robot exhibits stronger climbing ability and lower sensitivity to friction coefficients on vertical surfaces. This paper also achieved the implementation of the circuitry, software, and mechanical structure of the bipedal vertical surface cleaning robot. The designed robot incorporates functions like air quality detection, video information feedback, and wireless communication. Physical experiments confirmed that the robot can securely adhere to various vertical surfaces such as photovoltaic panels, painted walls, cabinets, and glass windows while effectively crossing obstacles. These results demonstrate that the developed robot is capable of cleaning photovoltaic panels, walls, cabinets, windows, and other vertical surfaces proficiently. Furthermore, with improvements in its signal acquisition mechanism and actuators, it can undertake more challenging tasks like defect detection and repair on these aforementioned vertical surfaces.

Acknowledgement

This research was supported in part by the Horizontal Scientific Research Project of Xiamen University of Technology (grant ZK-HX22157) and Xiamen Key Laboratory of Frontier Electric Power Equipment and Intelligent Control. The authors would like to express their gratitude to the editor and anonymous reviewers for their valuable feedback and suggestions.

References

[1] SHIYUAN, B., YULIANG, W., FENG, X., DEYI, K. (2021). A Four-legged Wall-climbing Robot with Spines and Miniature Setae Array Inspired by Longicorn and Gecko. *Journal of Bionic Engineering*. Vol. 18, No. 2, pp. 292-305.

[2] QIU, S., WU, J., ZHAO, H., WANG, S., HU, Q. and YAN, R. (2022). Body Design of a Storage Tank Wall-climbing Robot Based on Magnetic Adsorption. *China Mechanical Engineering*, Vol. 33, No. 3, pp. 270-278.

[3] CHAOJIE, L., LIKE, C., XIAOHUI, X. (2019). Design and adsorption stability analysis

of wall climbing robot based on wheeled magnetic adsorption for ultrasonic detection. *Journal of Central South University (Science and Technology)*, Vol. 50, No. 12, pp. 2989-2997.

[4] JUNFENG, L., XIAOWEI, H., YONG, C., et al.. (2022). The optimization design on the permanent magnetic wheel of a wall-climbing robot for large steel structure inspection. *Manufacturing Automation*, Vol. 44, No. 1, pp. 46-50.

[5] ADRIÁN, P., MAHMOUD, T., JOSÉ, M.M., et al. (2019). Design of compact switchable magnetic grippers for the HyReCRo structure-climbing robot. *Mechatronics*, Vol. 59, pp. 199-212.

[6] YUNHUI, J., ZHIHONG, Z., HONG, H. (2017). Research on controller of wall-climbing robot based on ARM-Linux. *Journal of Electronic Measurement and Instrumentation*, Vol. 31, No. 9, pp. 1459-1466.

[7] QIANG, Z., XIN, L. (2019). Convolutional network-based method for wall-climbing robot direction angle measurement. *Industrial Robot: the international journal of robotics research and application*, Vol. 46, No. 6, pp. 863-869.

[8] ZHIZHONG, L., WEIJIE, W., JINPENG, C., et al. (2022). Stability and dynamics analysis of a four-legged magnetic adsorption wall-climbing robot. *Journal of Harbin Engineering University*, Vol. 43, No. 3, pp. 429-435.

[9] QIN, Y., DONG, S., PANG, R., XIA, Z., ZHOU, Q., YANG, J. (2020). Design and Kinematic Analysis of a Wall-climbing Robot for Bridge appearance Inspection. *IOP Conference Series, Earth and Environmental Science,* Vol. 638, No. 1, p. 012062.

[10] CHANG, Q., LUO, X., QIAO, Z., LI, Q. (2019). Design and Motion Planning of a Biped Climbing Robot with Redundant Manipulator. *Applied Sciences-Basel*, Vol. 9, pp. 3009.

[11] ENJIKALAYIL ABDULKADER, R., VEERAJAGADHESWAR, P., HTET LIN, N., KUMARAN, S., VISHAAL, S.R. AND MOHAN, R.E. (2020). Sparrow: A Magnetic Climbing Robot for Autonomous Thickness Measurement in Ship Hull Maintenance. *Journal of Marine Science and Engineering*, Vol. 8, pp. 469.

[12] FUKUI, R., YAMADA, Y., MITSUDOME, K., SANO, K., WARISAWA, S.I. (2020). HanGrawler: Large-Payload and High-Speed Ceiling Mobile Robot Using Crawler. *IEEE Transactions on Robotics*, Vol. 36, No. 4, pp. 1053-1066.

[13] QIAOLING, D., XINPO, L., YANKAI, W., SINAN, L. (2020). The obstacle-surmounting analysis of a pole-climbing robot. *International Journal of Advanced Robotic Systems*, Vol. 17, No. 6, pp. 1-20.

[14] YOO, S., JOO, I., HONG, J., KIM, J., KIM, H.S., SEO, T. (2020). Mechanical and Empirical Parameter Design on a Multi-wound Differential Pulley Winch for a Wall-Climbing Robot. *Precision Engineering and Manufacturing*, Vol. 21, No. 5, pp. 857-867.

[15] KIM, T., JEON, Y., YOO, S., KIM, K., KIM, H.S., KIM, J. (2017). Development of a wall-climbing platform with modularized wall-cleaning units. *Automation in Construction.*Vol. 83, pp. 1-18.

[16] HU, S., PENG, R., KAI, H., LI, J., CAI, J., ZHOU, W. (2018). Optimal Design and Experimental Study on Magnetic Adsorption Unit of Crawler-Type Wall-Climbing Robot. *Machinery & Electronics*, Vol. 36, No. 1, pp. 69-74.

[17] HONGXIA, G., XIONG, W. (2015). Research and Design on Magnetic Adhesion Mechanism with Heavy Load. *Control Engineering of China*, Vol. 22, No. 2, pp. 356-359.

[18] BOYANG, Z., ZIWEI, Z., JUN, O., et al. Exploration on Biped Climbing Robot Based on Vacuum Adsorbing. *Hydraulics Pneumatics & Seals*, Vol. 6, pp. 68-71.

[19] GUAN, Y., ZHU, H., WU, W., ZHOU, X., JIANG, L., CAI, C., ZHANG, L., ZHANG, H. (2013). A Modular Biped Wall-Climbing Robot With High Mobility and Manipulating Function.*IEEE/ASME Transactions on Mechatronics*, Vol. 18, No. 6, pp. 1787-1798.

[20] SONG, X., ZHANG, X., MENG, X., CHEN, C., HUANG, D. (2021). Gait Optimization of Step Climbing for a Hexapod Robot. *Journal Of Field Robotics*, Vol. 39, pp. 55-68.

[21] YAN, L., LUYING, Z., HAOYANG, S., et al. (2018). Locomotion Analysis for Hexapod Robot Based on Tripod Gait. *Journal of Qingdao University(Engineering & Technology Edition)*, Vol. 33, No. 3, pp. 38-42.

[22] JIECHANG, C., LIZHONG, Z., YANGYANG, B. (2016). Co-simulation of Gait for Biped Robot Based on ADAMS and MATLAB. *Journal of Changchun University of Science and Technology*, Vol. 39, No. 5, pp. 81-84.

[23] XI, C., QUNFEI, Z., PEISUN, M. (2006). A Closed-form Inverse Kinematics Solution of a Biped Robot. *Machinery & Electronics*, Vol. 12, 60-62.

[24] ZHENG, Y., WU, Z., MA, C. 2022. Structural Optimization of Small Diameter Deep Well Rescue Robot Based on Hyperworks-Optistruct. *Manufacturing Technology*, 22, 771-6.

[25] CEDZO, M., JOCH, R., TIMKO, P., HOLUBJÁK, J., CZÁNOVÁ, T., ŠAJGALÍK, M. 2023. Topology Optimization of Gripping Jaws of Industrial Robot. *Manufacturing Technology*, 23, 25-31.

[26] SONG, L., SUN, H., XU, K., SHI, X., ZHOU, Y. 2022. Path Planning under The Hull bottom of Painting Robot Based on Heuristic Multi-robot Cooperation in Ship Manufacturing. *Manufacturing Technology*, 22, 218-30.

[27] JUNHUA, L., HAIFEI, L., JINGLUN, L., et al. Global path planning for a biped wall-climbing robot in 3D wall environment. *Journal of Harbin Institute of Technology*, Vol. 52, No. 1, pp. 148-155.